Nano Energy 141 (2025) 111120

Contents lists available at ScienceDirect

Nano Energy

journal homepage: www.elsevier.com/locate/nanoen

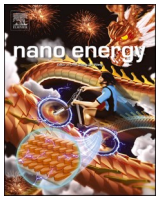

Hybrid energy harvester integrating ZnO piezoelectric nanogenerator with perovskite solar cell demonstrating the piezo-phototronic effect

Yuan Zhang [a], Xuan Li [b], Qinrong He [c], Madsar Hameed [a], Joe Briscoe [a,*]

[a] School of Engineering and Materials Science, Queen Mary University of London, London E1 4NS, UK
[b] Helmholtz-Zentrum Berlin, Berlin 12489, Germany
[c] Key Laboratory of Bionic Engineering (Ministry of Education), College of Biological and Agricultural Engineering, Jilin University, Changchun, Jilin 130022, China

ARTICLE INFO

Keywords:
ZnO based piezoelectric nanogenerator
Pervsikte solar cell
Hybrid energy harvest
Pizeo-phototronic effec

ABSTRACT

As portable devices and wireless sensors become more ubiquitous and power hungry, new methods are required to power them to avoid an overreliance on batteries. Materials that combine multiple functionalities, such as semiconducting and piezoelectric properties, offer an excellent opportunity to harvest energy from multiple sources in a single device. As such, we report a hybrid energy harvester (HEH) combining a piezoelectric nanogenerator and a perovskite solar cell to simultaneously harvest mechanical and solar energy. The HEH exhibited the piezo-phototronic effect, where strain-induced shifts in the energy bands of ZnO nanorods modulated the photovoltaic (PV) output under mechanical deformation. The output of the HEH under light and oscillation conditions combined PV variations driven by the piezo-phototronic effect and piezoelectric signals generated by the ZnO nanorods. Furthermore, the piezoelectric output showed distinct variations between dark and illuminated conditions, attributed to differences in the electrical conductivity of ZnO and perovskite, which influenced charge screening. Additionally, morphological variations in ZnO nanorods were found to significantly impact performance. Overall, these findings provide guidance for optimizing nanostructures and device designs to enhance multi-source energy harvesting efficiency and further explore the piezo-phototronic effect.

1. Introduction

Mechanical energy is the one of the most abundant and accessible energy sources, and has been widely harvested by large-scale technologies such as wind power or tidal stream generators. Piezoelectric nanogenerators (PENGs) provide a potential way to convert small mechanical energy such as body motion or vibration into electricity, which can be used to power small portable electronics, medical bio implants, remote wireless sensors etc. [1-3]. At the same time, solar energy offers the potential to provide much higher power levels than motion since the sun delivers more energy to the earth in 1 h than the entire planet consumes in one year [4]. However, light is not always available, nor is movement, therefore a hybrid energy harvester (HEH) combining PENGs and solar cells (SCs) that can make use of both sources provide a more reliable and high-level of power for small, portable or self-powered devices.

Zinc oxide (ZnO) has become a key material in HEH that combines PENG with photovoltaic (PV) solar cells [5]. Its wide bandgap, high electron mobility, excellent chemical stability, and tunable nanostructures enable ZnO to function as both a piezoelectric potential source in the PENG unit [6,7] and an electron transport layer (ETL) in the PV unit [8–10]. Hybrid systems integrating ZnO-based PENGs with solar cells have been widely explored to harvest both mechanical and solar energy [11–18]. The first ZnO PENG/SC HEH was reported by Xu et al [11]. in 2009, composed of a serially integrated 'zigzag' ZnO PENG and dye-sensitized solar cell (DSSC), achieving the piezoelectric output of 9 mV and a PV power conversion efficiency (PCE) of 0.76 %. Such designs utilized stacked layer structures, with the PENG and SC components operating independently on a shared silicon substrate as an electrode, but they faced challenges including complex assembly, short-circuit risks, and limited flexibility [11,12]. Subsequently, single-volume layer HEHs were reported by Choi et al. that combined ZnO PENG with organic solar cell (OSC), allowing more integrated operation and improving performance [14,15]. Among such OSC-PENG HEH designs, the maximum achieved piezoelectric output was 0.8 V and maximum PV PCE was 1.5 % [15,16]. The highest-performing HEH to date was reported by Liu et al [18]. that combined the ZnO PENG with amorphous-Si:H single junction solar cell, achieving the piezoelectric

* Corresponding author.
E-mail address: j.briscoe@qmul.ac.uk (J. Briscoe).

https://doi.org/10.1016/j.nanoen.2025.111120
Received 16 December 2024; Received in revised form 25 April 2025; Accepted 7 May 2025
Available online 9 May 2025

output of 3 V and a PV PCE of 2.96 %. Additionally, the strain-induced piezo potential can modulate the band structure of ZnO, which promotes the separation and transport of charge carriers generated in the light absorption layer [19,20]. Such synergistic effects between PENG and SC units, named the piezo-phototronic effect [21], have been shown to enhance solar cell efficiency under mechanical strain and widely studied in photodetectors [22], light-emitting diodes [23], and photocatalysis [24].

Despite these advancements, current HEHs still struggle with limited output power and energy conversion efficiency, primarily because the photovoltaic unit remains relatively inefficient. The three solar cell types mentioned earlier not only have inherently limited efficiency ceilings but also struggle to reach high PCE in practical applications (with record PCE of 13.0 % for DSSC, 19.2 % for OSC, and 14.0 % for a-Si:H) [16]. This highlights the need for more efficient photovoltaic materials and optimized device architectures to improve overall energy harvesting performance. Perovskites are an ideal photovoltaic component in such configurations due to their high PCE, solution-processed fabrication method, and compatibility with flexible substrates. After the first report by Miyasaka's group in 2009, the PCE for a single junction perovskite solar cell devices has increased from 3.8 % to 26.7 % [25,26], making it the fastest advancing PV technology to date. Additionally, PSCs are highly compatible with a flexible device architecture and show good durability under continuous bending, makes it an excellent candidate for hybrid devices to collect the mechanical energy [27]. However, no study has yet explored the use of perovskite as the photovoltaic component in HEH systems, and our work effectively fills this gap. Furthermore, the working mechanism of HEH during operation under illumination and strain are not yet fully understood, necessitating further investigation.

Therefore, here we combine a ZnO nanorod based PENG with a perovskite solar cell to create a HEH capable of simultaneously or separately harvesting dual mechanical and solar energy, achieving the highest reported PV PCE and piezoelectric power output among HEH devices to date. Through the systematic study of working mechanism of HEH, it was found that the piezoelectric output of HEH differs between dark and illuminated conditions mainly due to the varying conductivity of the perovskite layer under these conditions, altering the screening mechanism within the device. The output of the HEH under light and oscillation conditions consisted of a combination of the PV output variation due to the piezo-phototronic effect and the piezoelectric output arising from ZnO nanorods. ZnO nanorods with different aspect ratio were also employed to investigate the effect of morphology on both PV and piezoelectric output.

2. Method

2.1. Synthesis of ZnO nanorod

Substrates were first coated with a ZnO seed layer using a precursor solution consisting of 0.1 M zinc acetate ($Zn(CH_3COO)_2{\cdot}2H_2O$, $\geq$ 98 %, Sigma-Aldrich) and 0.1 M 2-amino ethanol ($NH_2CH_2CH_2OH$, 99 %, Sigma-Aldrich) in 2-methoxyethanol ($CH_3OCH_2CH_2OH$, 99 %, Sigma-Aldrich). The solution was stirred overnight and filtered with a 0.45 μm PTFE filter before deposition. 1.5 × 2.5 cm^2 PET/ITO (poly ethylene terephthalate/indium tin oxide) substrates were washed with water, acetone and 2-propanol, then treated with an oxygen plasma. 100 μl of precursor solution was drop casted on the PET/ITO substrate and spin coated at 500 RPM for 10 s followed by 3000 RPM for 30 s. Afterwards, the films were annealed at 140 °C for 30 mins and cooled down to finish one cycle. The same cycle was repeated five times. For the second, third and fourth cycle, the final annealing condition was 140 °C for 15 min. Four substrates were attached to a microscope slide using polyimide (Kapton) high temperature tape. The slide was immersed face down in an aqueous solution of zinc nitrate ($Zn(NO_3)_2{\cdot}6\ H_2O$, 99 %, Alfa Aesar) and hexamethylenetetramine ($C_6H_{12}N_4$, 99 %, Alfa Aesar, HMT) and was sealed in a jar. Two different growth methods were operated to get different ZnO morphology. Method '0.06' used the precursor solution with the concentration of 0.06 M of zinc nitrate and HMT, and grew at 85℃ for 1.5 h. Method '0.025' using the precursor solution with the concentration of 0.025 M, and grew at 90℃ for 2.5 h. After growth the substrate was washed with DI water and dried at 50 °C for 15 min.

2.2. Fabrication of hybrid energy harvester

Perovskite ($CH_3NH_3PbI_3$: $MAPbI_3$) precursor solution was prepared by dissolution of CH_3NH_3I with PbI_2 in DMF:DMSO mixed solvent (9:1.1, volume ratio) stirring for 15 min. The 1.5 M $MAPbI_3$ precursor solution was filtered with 0.45μm PTFE filter before use. Before the deposition, the ZnO nanorod films were annealed for 1 hour at 150 °C and treated with oxygen plasma treatment for 30 minutes to remove the residual hydroxyl group and reduce the surface defects. 50 μl of perovskite precursor solution was dripped on the ZnO nanorods film and spin coated at 4000 RPM for 20 s. Diethyl ether, as the anti-solvent, was dripped during the sixth and seventh second during the spin-coating process. Afterwards, the films were annealed at 100 °C for 20 mins. Solution of hole transport material was prepared by dissolving 10 mg of Poly(triaryl amine) (PTAA, Mw = 14,000, Ossila) in 1 ml toluene and was stirred for 1 h at 65℃. The solution was then doped with additives of 3.8 μL bis(trifluoromethane)sulfonimide lithium salt (Li-TFSI)/acetonitrile (340 mg ml^{-1}, TCI) and 3.8 μL of 4-tert-butylpyridine (tBP, TCI). The doped PTAA was filtered through a 0.45 μm PTFE filter before use and spin-coated onto the perovskite films at 3000 rpm for 30 s. PMMA in anisole solution was painted on the left corner of substrate, as the insulating layer. Au electrode of 150 nm thickness was deposited by high vacuum thermal evaporation. Copper tapes were stuck to the ITO and Au layer as the electrodes. Silver epoxy was painted on the connection to improve the conductivity. The device was encapsulated in a laminating pouch by hot press. The deposition of perovskite film and HTL layer were conducted in a glovebox and all other steps were conducted in ambient conditions. The fabrication process is displayed in Figure S1a-g.

2.3. Characterizations and measurements

The piezoelectric performance (output voltage and power resulting from mechanical bending of the device) was tested using a bespoke setup consisting of a frequency generator, magnetic shaker (Brüel & Kjær, LDS V406), variable resistance box (100 Ω to 10 MΩ) and data acquisition system. The vibration from the magnetic shaker was used to induce bending in the device by utilizing a resonant mass-spring system, formed by a spring steel cantilever with a tip mass (30 g), on which HEH was attached, as shown in Figure S1i. By changing the frequency and amplitude of the shaker and the cantilever length, the spring steel can reach its resonance frequency and the device can obtain maximum output. All devices were tested using an identical cantilever and tip mass arrangement to maintain consistent bending conditions between samples. The corresponding voltage output was monitored by a Tektronix TDS2012C oscilloscope in trigger mode. The HEH was connected to a 3.3 μF capacitor to demonstrate its energy harvesting and storage capabilities under light and oscillation. A bridge rectifier was used to convert the alternating current (AC) generated from the ZnO piezoelectric effect into direct current (DC) for efficient storage. The voltage during the charging of capacitor and the PV performance was measured by a Kiethley 2400 SMU with LabVIEW 8.0 software and tested under 1 sun (100 mW/cm^2) provided by a Newport solar simulator apparatus. Fixed strain was introduced to HEH device by attaching the device to templates with different bending radii. ZnO nanorod and perovskite films were characterized using scanning electron microscopy (SEM) (FEI Inspect-F). The surface morphology of films was characterized at 5 kV and the cross-section was measured at 20 kV. The working distance used was 10 mm. Impedance analysis was measured using a potentiostat (Interface 1000, Gamry instrument) from 1 to 10^6 Hz under different

condition (dark, room light and 1 sun illumination), where the intensity of office lighting for the room light condition was measured as 380 lux. UV–Vis spectroscopy was recorded on a UV–vis–NIR spectrometer (Lambda 950), and diffuse reflectance spectra and transmittance spectra were measured with an integrating sphere. Grazing Incidence X-ray diffraction (GIXRD) was measured by an Xpert-Pro diffractometer with Cu/Kα radiation (PANalytical, Netherlands), and the data were collected from 5° to 70° with the incidence angle of 0.5°. Photoluminescence spectroscopy was measured with a FLS 1000 from Edinburgh instruments, illuminated by a Xenon lamp at the excitation wavelength of 405 nm, with step-size of 1 nm. Time-resolved photoluminescence spectroscopy measured using a picosecond pulsed diode laser at the excitation wavelength of 375 nm.

3. Result and discussion

The HEH device was fabricated with the structure of PET/ITO/ZnO nanorod/$MAPbI_3$/PTAA/Au as shown in Fig. 1a. The ZnO seed layer was deposited on the PET/ITO substrate by spin coating and ZnO nanorods were grown at 85C for 1.5 h in a precursor solution with a concentration of 0.06 M of zinc nitrate and HMT. The perovskite and hole transport layer (PTAA) were deposited by spin coating afterward and the Au layer was deposited by thermal evaporation as the contact electrode. The vibration from the magnetic shaker induced bending in the device through a resonant mass-spring system, consisting of a spring steel cantilever with a 30 g tip mass supporting the attached HEH. The output signal was recorded by connecting HEH to an oscilloscope, while adjusting the shaker's frequency allowed the system to reach its resonance frequency for maximum output. (Figure S2) The HEH device can simultaneously and separately harvest both mechanical and solar energy, as proved by the output voltage signal of HEH under dark and light condition shown in Fig. 1b. The HEH provided a stable photovoltaic output (V_{PV}) under 1 sun illumination, and voltage spikes corresponding to the maximum amplitude of bending of the cantilever at resonant frequency. V_{max} refers to the maximum voltage point under the oscillation condition while peak voltage (V_{peak}), which is the piezoelectric voltage output of HEH, referred to as the nanogenerator (NG) output, is obtained from the peak difference between the baseline and V_{max}. For dark oscillation condition, $V_{peak} = V_{max} = 1.36$ V. For light oscillation condition, V_{peak} is calculated by subtracting the PV output from the voltage peak under combined light and mechanical excitation, which give 1.84–0.9 = 0.94 V. The performance of HEH was also proved by charging a capacitor of 3.3 μF under light or/and oscillation condition. (Figure S3). For comparison, equivalent devices using SnO_2 and ZnO as ETL instead of ZnO nanorod shows PV output, but no signal under oscillation. (Figure S6a and c) This confirmed that the NG output arose from the piezoelectric property of the ZnO nanorods.

There is no obvious degradation in the output piezoelectric voltage during durability testing shown in Figure S4a and b. However, the PV output does decrease steadily after around 10,000 cycles, reaching around 40 % of its original performance after 50,000 cycles (Figure S4c). Such degradation of PV performance does not occur under illumination only, without bending (Figure S4d). This suggests that some mechanical failure of the device may be occurring, potentially at the ZnO/perovskite interface, which is not sufficiently severe to affect the piezoelectric voltage output but does impact the PV performance [28]. Thus further investigation and optimisation of the mechanical stability of such HEH devices would be an important avenue for future research.

The PV performance of HEH device was tested under 1 sun illumination and summarised in Table 1. Compared with performance of solar cell device using SnO_2 and ZnO as ETL (Figure S6 and Table S1), the relatively low PCE may result from surface defects on ZnO nanostructures, which induced non-radiative charge carrier recombination. The structural requirements for test wire integration of the HEH, diverging from the direct electrode contact typical in traditional

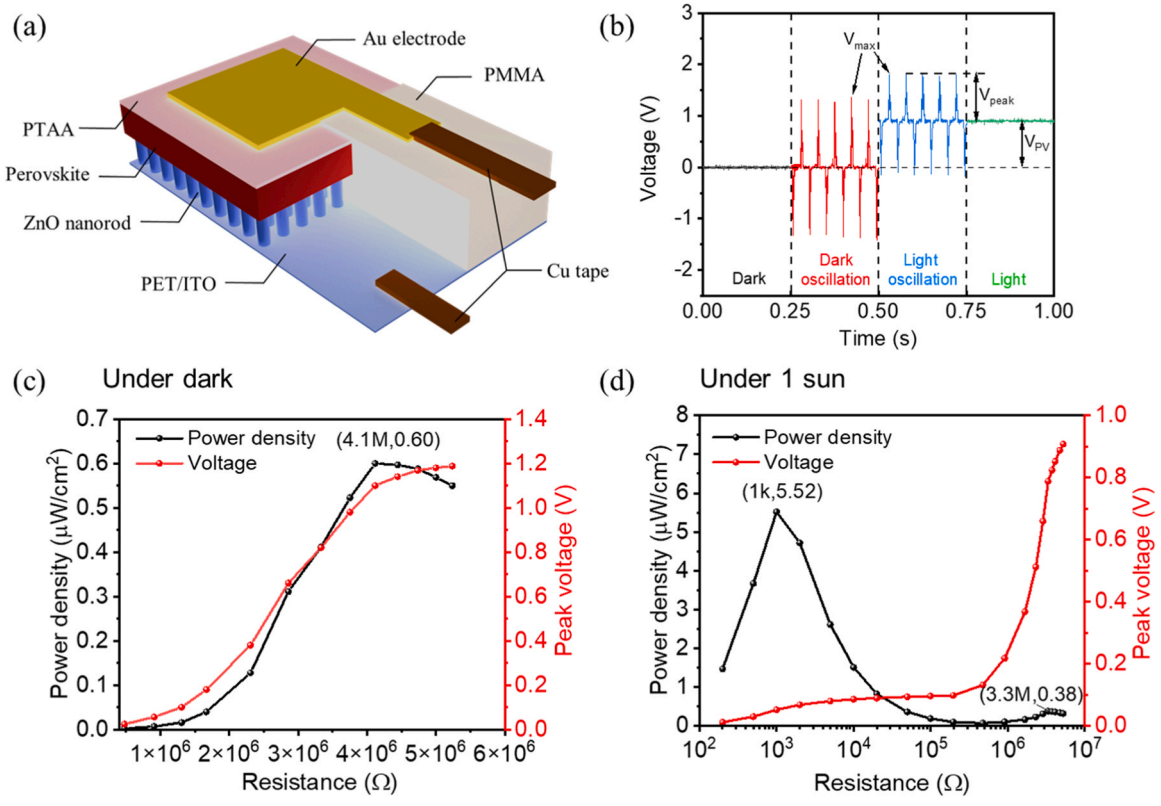

Fig. 1. (a) Schematic of the structure of hybrid energy harvester. (b) The output signal of hybrid energy harvester under 1 sun illumination and oscillation. (c-d) The power density-load resistance-Voltage (P-R-V) plot of hybrid energy harvester device tested under (c) dark condition and (d) 1 sun illumination.

Table 1
The photovoltaic performance of hybrid energy harvester.

Scan	PCE (%)	FF (%)	J_{SC} (mA/cm^2)	V_{OC} (V)
Forward	3.60	48.25	8.29	0.90
Reverse	4.20	53.61	8.65	0.91

perovskite solar cells, also diminished efficiency. Additionally, the large electrode area and relatively high sheet resistivity can be detrimental to performance. However, despite these challenges, the device clearly functions as a working solar cell, with output that is sufficient to investigate the operating mechanisms, as well as clearly providing additional power output compared to a NG operating on its own.

To investigate the power output of the device under different operating conditions, the nanogenerator performance of HEH device was first assessed by connecting it in parallel to the resistors and simultaneously recording the voltage output. The output power, P, was calculated as [29]:

$$P = \frac{V^2}{R_{eq}}$$

$$R_{eq} = \frac{R_{external} \cdot R_{oscilloscope}}{R_{external} + R_{oscilloscope}}$$

where $R_{external}$ is the external load resistance, which varied from 100 Ω to 10 MΩ; $R_{oscilloscope}$ is the input resistance of oscilloscope, which is 10 MΩ; R_{eq} is the equivalent resistance which is calculated based on the parallel connection of $R_{oscilloscope}$ and $R_{external}$; V is the measured V_{peak} at the set resistance. For the measurement conducted under light, V_{peak} is calculated by subtracting the stable PV output from the voltage peak as discussed before (and shown in Fig. 1b) in order to isolate only the peak associated with the NG output. Then, the maximum output power (P_{max}) can be obtained by varying the external resistance. As shown in Fig. 1c, under dark condition, HEH obtained a piezoelectric output of 0.60 μW/cm^2 when connected with an equivalent resistance of 4.1 MΩ. However, under the 1 sun illumination shown in Fig. 1d, two maxima are observed in the P-R curve, located at 1 kΩ and 3.3 MΩ, achieving 5.52 and 0.38 μW/cm^2, respectively. P_{max} obtained at 3.3 MΩ was assumed to arise from the piezoelectric output of ZnO nanorod due to the similar external resistance to that of P_{max} in the dark. Therefore, compared with the output under dark condition, under 1 sun illumination the piezoelectric contribution to the HEH device achieved a lower P_{max} (0.38 compared to 0.60 μW/cm^2) at the lower external resistance (3.3 compared to 4.1 MΩ).

The lower piezoelectric output under light was attributed to photoexcitation of the ZnO and perovskite layer under light, which increases the carrier density and therefore conductivity, thus increasing the screening effect. The screening effect refers to the reduction of output due to the transfer of free charge carriers that neutralize the generated piezoelectric potential internal electric field [30,31]. As the ZnO nanorods deform, a polarization-related electric field arises between the two ends of the ZnO nanorods, which induces the movement of free charges within the ZnO nanorod (internal screening effect) as well as in adjacent materials (external screening effect). Such screening charges moves simultaneously with the build-up of polarization during the deformation of ZnO nanorods, which then neutralise the polarization-related electric field. It was reported that the carrier density of ZnO can be increased by 2–3 orders of magnitude under light illumination [32]. This was attributed to the semiconducting nature of ZnO, whose wide bandgap of 3.29 eV, (Figure S9a) enabled UV light absorption [33], electron-hole pair generation, and a substantial increase in conductivity. The perovskite $MAPbI_3$ with a bandgap of 1.59 eV (Figure S9b) enables broad absorption in the visible range [34–36], leading to a reported 5–6 orders of magnitude increase in carrier density under illumination [37]. Therefore, the increase of conductivity of ZnO and perovskite enhanced the internal and external screening, respectively, resulting in the reduction of piezoelectric output. To test this hypothesis, a PENG with structure of PET/ITO/ZnO nanorod/PEDOT:PSS/Au was fabricated to compare with the HEH and the impedance analysis was conducted on the HEH and ZnO PENG to study the internal resistance of the devices without and with illumination. In Figure S7, the output of PENG was slightly reduced from 0.248 μW/cm^2 (in the dark) to 0.225 μW/cm^2 (under illumination), due to the improved conductivity of ZnO under illumination as proved by the reduced internal resistance of PENG under illumination (Figure S8b). The improved conductivity of ZnO nanorods induced an internal screening effect and resulted in the voltage loss during oscillation. The internal resistance of HEH dramatically decreased from 30.38 to 2.94 kΩ when exposed to room light condition, and further decreased to 159 Ω under 1 sun illumination (Figure S8c). The greater reduction in internal resistance of HEH compared to ZnO PENG further confirmed the significantly higher carrier density increase in perovskite, which was primarily attributed to its lower bandgap. The increased photoconductivity increased the external screening effect, resulting in reduced piezoelectric voltage and power output. Therefore, the reduction in the piezoelectric voltage and power output of HEH under illumination was attributed to the photoexcitation of ZnO and perovskite layer, which largely increased the conductivity and enhanced the internal and external screening effects.

To further study the mechanism of operation of the HEH and uncover the underlying origin of the peak in P_{max} achieved at 1 kΩ in Fig. 1d, the behaviour of HEH devices under light, bending and fast flicking/oscillating conditions was analysed step-by-step with reference to the associated changes in the energy band diagrams. The HEH device went through five processes during this test: (i) steady state (SS); (ii) slow bending (SB); (iii) holding (HD); (iv) fast release (FR) and (v) back to steady state under room light illumination. To describe the direction of bending, the PET side was considered as the front side of device, as the PET side needs to face up to harvest light. Fig. 2 displays the voltage and current signal and the corresponding energy band diagrams during the downward bending and release test. A heterojunction is formed between ZnO and perovskite, and under illumination, electrons are excited from the valence band to the conduction band of perovskite. The photogenerated electron-hole pairs are separated by the internal electric field at the depletion region, with electrons transferring to ZnO (blue curve arrow at the ZnO/perovskite interface in Fig. 2c) and holes to the hole transport layer. Therefore, during the steady state process (i) in Fig. 2c, the HEH produced a stable PV output (V_{PV}). When the HEH device was slowly bent (ii), the voltage and current output of HEH under light slowly increased to an elevated level (V_{EPV}, elevated PV output) when held at downward bending (iii). This enhancement can be attributed to the piezo-phototronic effect of the ZnO nanorods/perovskite structure. Under the downward bending condition, the ZnO nanorods experience tensile strain and the electrons accumulate at the bottom of nanorods, which induced a positive piezoelectric potential at the interface between ZnO nanorods and perovskite layer. The positive potential lowers the energy level of ZnO and reduces the barrier height for electron transfer from the perovskite to ZnO as shown in blue curve arrow in Fig. 2d, which can expedite the separation of the electron–hole pairs and suppress recombination, resulting in the enhanced PV output. To support the hypothesis of the contribution from the piezo-phototronic effect, the J-V curve for HEH under varied fixed tensile strain is displayed in Figure S10. Similarly, the ZnO nanorods experience compressive strain when upward bent, the negative piezoelectric potential raised the energy level of ZnO as shown Figure S11d, which increased the barrier height and resulted in a reduced PV output. During the slow bending process (ii), the NG signal was not observed because slow bending allows plenty of time for internal screening and therefore the potential difference is effectively neutralized by mobile charges. In contrast, during the fast bending and release process, a pulsed NG signal can be observed, as displayed Fig. 1b. The rapid deformation does not provide sufficient time for the electrons to fully redistribute and

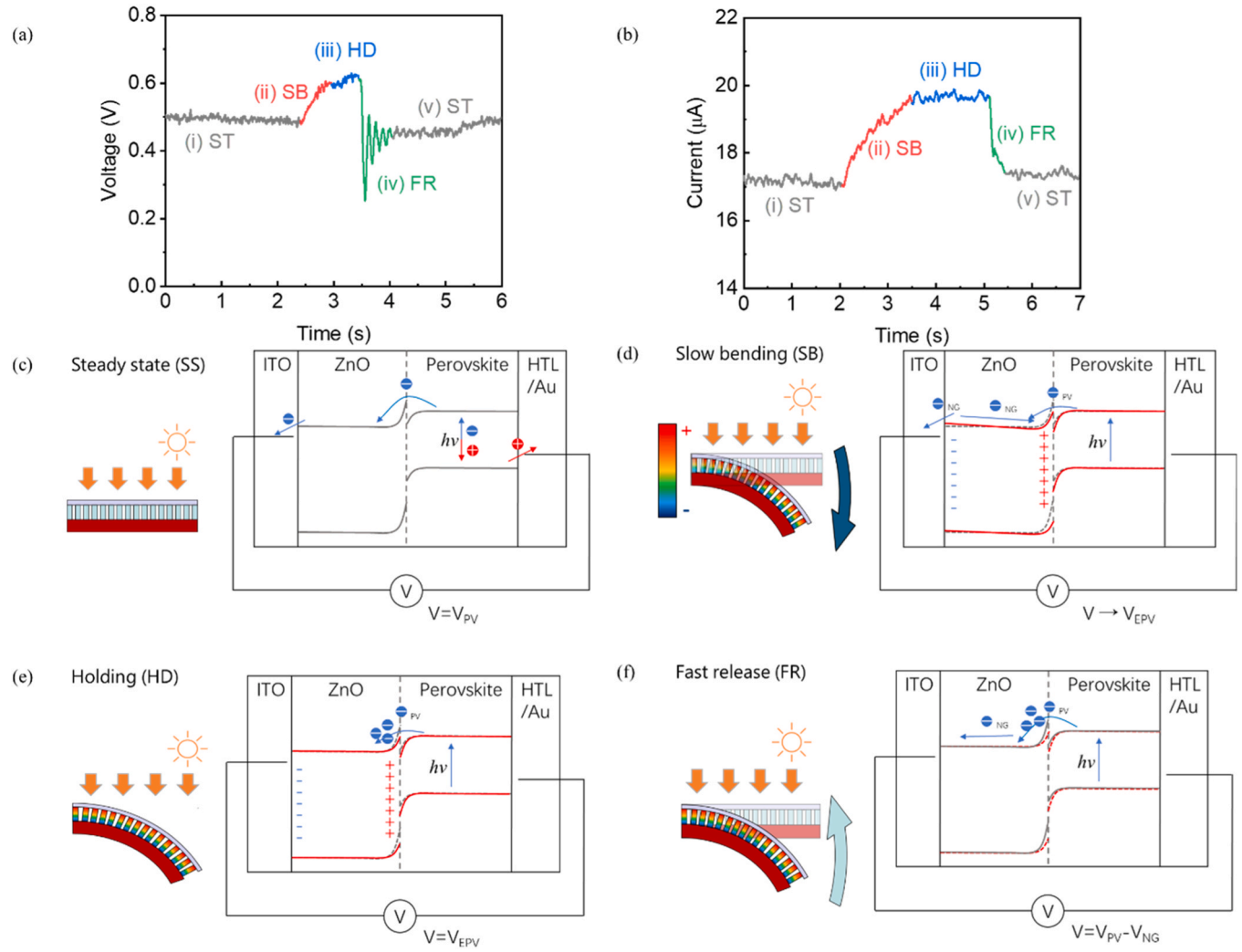

Fig. 2. (a) The voltage and (b) current signal of hybrid energy harvester during the downward bending test under room light. (c)-(d) The (i) steady state (SS); (ii) slow bending (SB); (iii) holding (HD); (iv) fast release (FR) state of hybrid energy harvester. The energy band diagrams at corresponding state with the dashed lines showing the equilibrium band positions, and red solid lines the altered band position resulting from the redistribution of screening charges in the ZnO (the piezotronic effect).

neutralize the piezoelectric potential. During the fast release process (iv), the HEH device vibrated several rounds and returned to the unstrained state. The piezoelectric potential disappeared due to fast disappearance of deformation, and the electrons that had not yet been transferred formed an electric potential as shown in Fig. 2f, which produced a piezoelectric signal shown in fast release process (iv) of Fig. 2a. When the electrons were fully transferred back to the bottom of ZnO nanorod, the potential vanished and HEH system returns to the stable state (v). However, such signal was not observed in the current. (Fig. 2b) This could be because the current output of the PENG is approximately two orders of magnitude lower than that of the solar cell. (Figure S12b and d) Based on these systematic tests, we can explain that the voltage signal from the HEH under light and oscillation conditions shown in Fig. 1b consisted of a combination of the PV output variation due to the piezo-phototronic effect during bending, and the piezoelectric output arising from the ZnO nanorods. This also explains the peak P_{max} observed at 1 kΩ for the HEH under illumination, which could be attributed mainly to the piezo-phototronic enhancement of the PV response under oscillation, as considered in the following discussion. For the HEH oscillated in the dark condition (Fig. 1c), as the connected resistance decreased, V_{peak} rapidly decreased to 0.024 V at 0.5 MΩ. For the HEH oscillated under 1 sun illumination (Fig. 1c), V_{peak} similarly decreased as resistance fell from 5 MΩ to 1 MΩ, but remained at around 0.1 V from 1 MΩ to 1 kΩ (Figure S13). The voltage baseline corresponded to the output voltage of the PV component. When the external resistance exceeded 1 kΩ, it closely approached the open-circuit voltage of the PV. As the external resistance was reduced to 200 Ω, the PV voltage output decreased, as shown in the J-V curve. Thus, we propose that the V_{peak} observed in the 1 MΩ to 1 kΩ range, staying around 0.1 V, results from PV output variation during oscillation due to the piezo-phototronic effect. As the external resistance is decreased further below 1 kΩ, the PV voltage variation decreased with the decrease of PV output voltage, and therefore the second P_{max} of 5.52 μW/cm^2 was obtained at 1 kΩ. In summary, at resistances above 1 MΩ, the piezoelectric output dominates V_{peak}, whereas below 1 MΩ, the PV output variation under oscillation due to the piezo-phototronic effect becomes more significant.

Having identified that there are PV, NG and piezo-phototronic effects contributing to the output from the HEH, it is then interesting to investigate the effect of morphology of ZnO nanorod on the performance of HEH. Thus, ZnO nanorods with higher aspect ratio were employed in the HEH to compare to those of lower aspect ratio used in the studies above. To obtain the longer and thinner ZnO nanorod, a lower concentration growth solution (0.025 M) was used at a higher temperature for longer growth time [38,39]. As shown in Fig. 3b and f, ZnO nanorod fabricated with 0.025 M method (named as 0.025 ZnO nanorods)

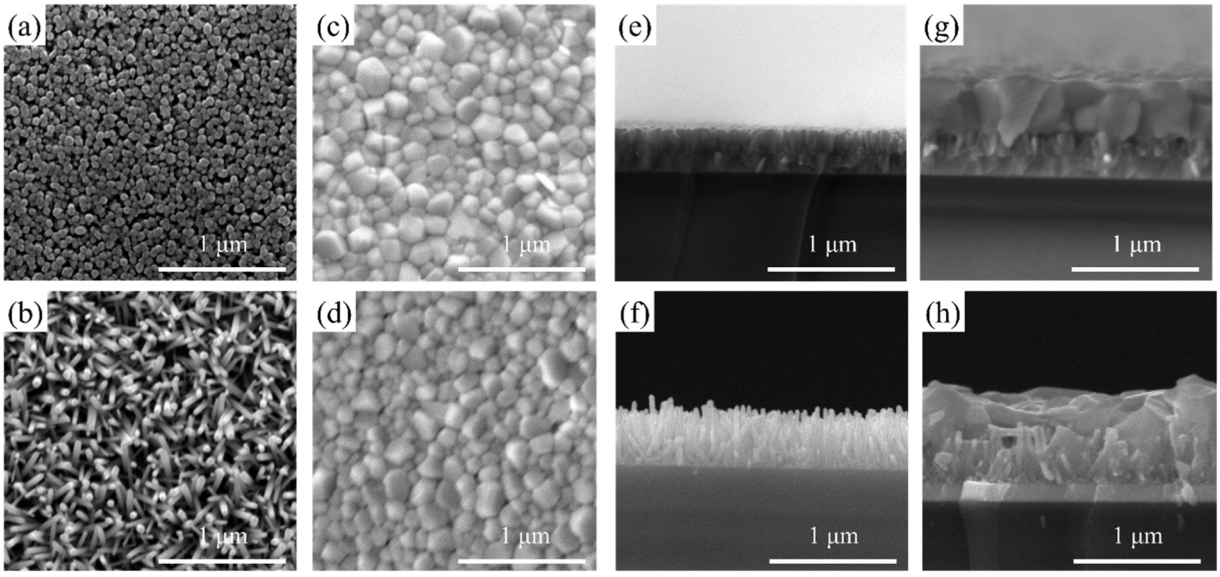

Fig. 3. (a-d) Top view SEM micrographs of (a) ZnO nanorods film grown with 0.06 M method; (b) ZnO nanorods film grown with 0.025 M method; (c) perovskite/ZnO nanorods film grown with 0.06 M method; (d) perovskite/ZnO nanorods film grown with 0.025 M method. (e-h) Cross-section SEM micrographs of (e) ZnO nanorods film grown with 0.06 M method; (f) ZnO nanorods film grown with 0.025 M method; (g) perovskite/ZnO nanorods film grown with 0.06 M method; (h) perovskite/ZnO nanorods film grown with 0.025 M method.

achieve a higher aspect ratio of 8.36 compared with 2.73 of 0.06 M method (named as 0.06 ZnO nanorod, used in the studies above). The diameter distribution of ZnO nanorod is displayed in Figure S14. When using the 0.025 nanorods, some pinholes can be observed between the grain boundaries of the perovskite crystal (Fig. 3d), because the ZnO nanorods film was highly rough, offering a less ideal surface for perovskite film growth. The 0.06 perovskite film showed much fewer pin holes (Fig. 3c), mainly due to the denser 0.06 ZnO nanorod film shown in Fig. 3a. From the cross-section SEMs in Fig. 3h, it can be seen that the perovskite layer was fully immersed into the 0.025 ZnO nanorods. However, in the case of 0.06 nanorods, the perovskite layer was just deposited on the top of nanorods (Fig. 3g), because of the denser 0.06 ZnO nanorods. The parameters of ZnO nanorods and perovskite are summarized in Table S3. The GIXRD pattern (Figure S15) confirmed the successful growth of ZnO nanorod and deposition of perovskite layer. Specifically, for 0.06 ZnO nanorod, (002) is stronger than (100) and (101), whereas for 0.025 ZnO nanorod, (002) is weaker than (100) and (101) due to a relatively lower degree of alignment along the c-axis of the 0.025 ZnO nanorod. A small PbI_2 peak which indicate the degradation of perovskite can be observed in both films.

The 0.025 HEH achieved a PCE of 7.37 %, which represents the highest efficiency reported to date for PENG/SC HEH. (Table S4 and Table S5) Compared with 0.06 HEH, the higher PCE of 0.025 HEH was mainly due to higher J_{SC} (Fig. 4a, and Figure S16). From the UV-Vis spectra (Figure S17), there was no significant difference in the transmittance and reflectance of PET/ZnO nanorod made from different method, indicating that the both ZnO did not affect the transmission of light. Additionally, the light absorbance of perovskite/0.025 nanorods is comparable to that of the 0.06 nanorods, suggesting similar light absorption capabilities. Therefore, the enhancement in J_{SC} primarily resulted from the improved connection between the perovskite film and 0.025 ZnO nanorods, due to the complete immersion of perovskite within the ZnO nanorods shown in Fig. 3h. Impedance analysis was performed on HEH devices fabricated using both 0.025 and 0.06 ZnO nanorods to investigate charge transport across the ZnO/perovskite interface. As shown in Fig. 4b, the HEH device made from 0.025 nanorod obtained a lower internal resistance of 15.47 kΩ compared with the 0.06 nanorod device which has an internal resistance of 30.37 kΩ. This indicated the better charge transport for 0.025 ZnO nanorod/perovskite interface due to the full immersion of perovskite. Steady-state photoluminescence (PL) emission and time-resolved photoluminescence (TRPL) analysis were conducted to further investigate the charge carrier dynamics of $MAPbI_3$ deposited on 0.025 and 0.06 ZnO nanorods. In Fig. 4c, the lower steady-state PL intensity observed with the 0.025 ZnO nanorod/perovskite film indicated a more significant PL quenching effect compared to the 0.06 ZnO nanorod, suggesting enhanced charge collection at the interface. The TRPL spectra shown in Fig. 4d illustrated that the decay dynamics of perovskite film on ZnO nanorod are bi-exponential, including a fast-decay phase (τ_1) attributed to the monomolecular charge trapping, and a slow-decay phase (τ_2) attributed to the bimolecular radiative recombination. (Table S6) The fast decay time (τ_1) for perovskite film on 0.025 (11.41 ns) and 0.06 (12.17 ns) nanorods was very similar, which indicated the similar perovskite film quality made on these two methods. However, the slow decay time (τ_2) for the 0.025 nanorod (106.71 ns) was significantly faster than that of the 0.06 nanorod (166.87 ns), indicating the faster electron transfer. The accelerated electron injection rate from the perovskite to the ZnO nanorod ETL promoted charge separation and effectively mitigated charge recombination at the perovskite/ETL interface. This phenomenon led to higher J_{SC}, which is consistent with the J–V measurements.

The piezoelectric performance is summarized in Table 2, Figure S18 and Figure S19. The HEH made from 0.06 ZnO nanorod achieved higher voltage output and power density. This could be attributed to the higher ZnO nanorod layer density of the 0.06 nanorods compared with the 0.025 nanorods, and the improved vertical alignment of the 0.06 nanorods. The structural configuration at the ZnO-perovskite interface is also a potential factor influencing variations in piezoelectric performance. In Fig. 4e, where the perovskite layer is less immersed into 0.06 ZnO nanorod, the vertical orientation of the piezoelectric potential facilitates efficient charge separation, minimizing screening effects and enhancing NG performance. In contrast, Fig. 4f shows a more immersed perovskite layer, where the curved arrow suggests a stronger internal screening effect, leading to increased charge recombination and a lower NG output.

4. Conclusion

A ZnO nanorod/perovskite solar cell hybrid energy harvester device

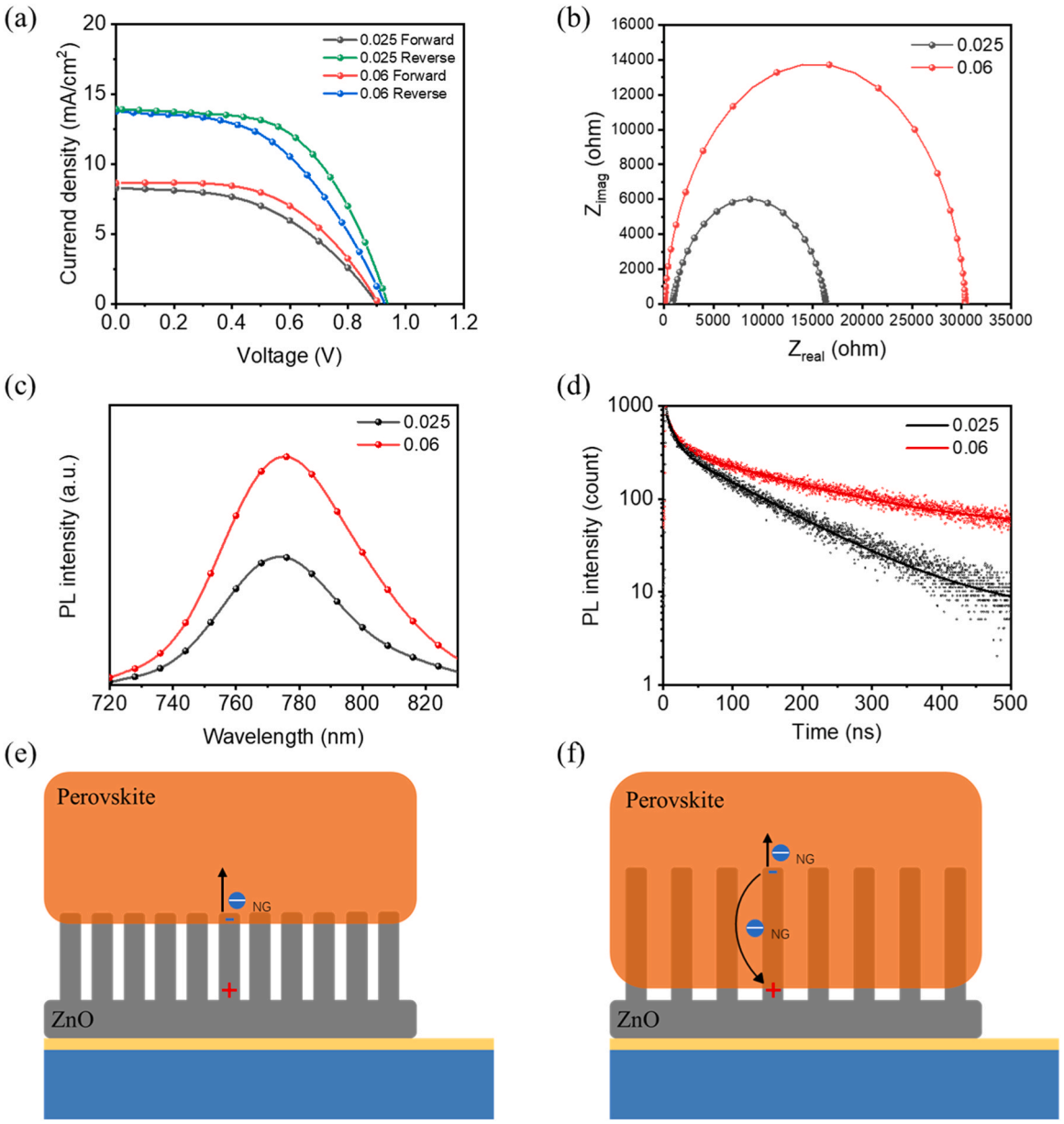

Fig. 4. (a) J-V curve of champion device of hybrid energy harvester fabricated with 0.025 and 0.06 ZnO nanorod; (b) Nyquist plots for hybrid energy harvester made by 0.025 and 0.06 method. (c) Steady state photoluminescence emission and (d) time-resolved photoluminescence spectra of perovskite film deposited on ZnO nanorods made by 0.025 and 0.06 method. (e) and (f) Schematics to show the potential charge transfer in hybrid energy harvester under bending.

Table 2
The champion device of HEH fabricated with 0.025 and 0.06 nanorod tested under 1 sun illumination and dark condition.

Method	Condition	Max Power density (μW/cm²)	Resistance at Pmax (Ω)	Piezoelectric voltage output (V)
0.025	Light	0.20	4.1 M	0.76
	Dark	0.34	4.1 M	1.20
0.06	Light	0.38	3.3 M	0.94
	Dark	0.60	4.1 M	1.36

was successfully fabricated that can simultaneously and separately harvest both mechanical and solar energy. The device achieved piezoelectric output of 1.36 V under dark and 0.94 V under 1 sun illumination. The reduced piezoelectric output under the light was attributed to the improved (photo)conductivity of ZnO and perovskite increasing the screening of the polarisation. The operational mechanisms of the HEH were explored, emphasizing the synergistic effects between the perovskite and piezoelectric ZnO nanorods. The PV output can be altered by mechanically bending the devices, because of the strain-induced shifting of the band energy levels in ZnO. The output of the HEH under light and oscillation conditions therefore consisted of a combination of the PV output variation due to the piezo-phototronic effect and piezoelectric output arising from the ZnO nanorods. Furthermore, ZnO nanorods with different aspect ratio were compared in HEH devices. The HEH device with lower aspect ratio, denser nanorods obtained higher piezoelectric output due to the larger deformation space and better nanorod alignment. The HEH device with thinner, longer nanorods obtained higher PCE (7.37 %) as a solar cell because of better interfacial connection between nanorod and perovskite layer. Further work can be focused on the enhancement of both piezoelectric and PV performance of HEH devices. Potential methods involve: optimizing aspect ratio and alignment of ZnO nanorod to achieve higher piezoelectric potential; ZnO

surface passivation and doping to supress the interface recombination and optimize the energy level alignment; improving perovskite and interfacial toughness to enhance stability under vibrations; and optimizing encapsulation strategies with moisture-resistant and stretchable materials to ensure long-term stability. Through these further studies it is also hoped that the mechanisms underlying the device behavior can be understood in more detail.

CRediT authorship contribution statement

Briscoe Joe: Writing – review & editing, Supervision. **Hameed Madsar:** Resources, Methodology. **He Qinrong:** Resources, Methodology. **Li Xuan:** Methodology, Investigation, Formal analysis, Conceptualization. **Zhang Yuan:** Writing – original draft, Validation, Software, Methodology, Investigation, Data curation, Conceptualization.

Declaration of Competing Interest

The authors declare that they have no known competing financial interests or personal relationships that could have appeared to influence the work reported in this paper.

Acknowledgements

Y.Z. acknowledges the support of the China Scholarship Council program (Project ID: 202008320300) and Queen Mary University of London CSC-QMUL joint PhD scholarship.

Appendix A. Supporting information

Supplementary data associated with this article can be found in the online version at doi:10.1016/j.nanoen.2025.111120.

Data Availability

Data will be made available on request.

References

[1] M.A. Parvez Mahmud, N. Huda, S.H. Farjana, M. Asadnia, C. Lang, Adv. Energy Mater. 8 (2018) 1701210.
[2] Q. He, J. Briscoe, ACS Appl. Mater. Interfaces 16 (2024) 29491–29520.
[3] D. Hu, M. Yao, Y. Fan, C. Ma, M. Fan, M. Liu, Nano Energy 55 (2019) 288–304.
[4] G.W. Crabtree, N.S. Lewis, Phys. Today 60 (2007) 37–42.
[5] H. Ryu, H. Yoon, S. Kim, Adv. Mater. 31 (2019) 1802898.
[6] Y. Zhang, Q. He, G. Tian, X. Li, C. Zeng, P. Ren, I. Abrahams, E. Bilotti, S. Dimitrov, A.J. Sobrido, J. Briscoe, J. Alloy. Compd. 1010 (2025) 177086.
[7] Y. Qiu, C. Bao, M. Gou, J. Zhao, D. Yang, Mater. Today Commun. 39 (2024) 108598.
[8] P. Zhang, J. Wu, T. Zhang, Y. Wang, D. Liu, H. Chen, L. Ji, C. Liu, W. Ahmad, Z. D. Chen, S. Li, Adv. Mater. 30 (2018) 1703737.
[9] J. Luo, Y. Wang, Q. Zhang, Sol. Energy 163 (2018) 289–306.
[10] P. Zhang, J. Wu, T. Zhang, Y. Wang, D. Liu, H. Chen, L. Ji, C. Liu, W. Ahmad, Z. D. Chen, S. Li, Adv. Mater. 30 (2018) 1703737.
[11] C. Xu, X. Wang, Z.L. Wang, J. Am. Chem. Soc. 131 (2009) 5866–5872.
[12] C. Xu, Z.L. Wang, Adv. Mater. 23 (2011) 873–877.
[13] M. Lee, R. Yang, C. Li, Z.L. Wang, J. Phys. Chem. Lett. 1 (2010) 2929–2935.
[14] D. Choi, K.Y. Lee, K.H. Lee, E.S. Kim, T.S. Kim, S.Y. Lee, S.-W. Kim, J.-Y. Choi, J. M. Kim, Nanotechnology 21 (2010) 405503.
[15] D. Choi, K.Y. Lee, M.-J. Jin, S.-G. Ihn, S. Yun, X. Bulliard, W. Choi, S.Y. Lee, S.-W. Kim, J.-Y. Choi, J.M. Kim, Z.L. Wang, Energy Environ. Sci. 4 (2011) 4607.
[16] Y. Kim, W. Kim, D. Choi, D. Choi, Int. J. Precis. Eng. Manuf. -Green. Technol. 9 (2022) 1077–1086.
[17] G.C. Yoon, K.-S. Shin, M.K. Gupta, K.Y. Lee, J.-H. Lee, Z.L. Wang, S.-W. Kim, Nano Energy 12 (2015) 547–555.
[18] G. Liu, N. Mrad, E. Abdel-Rahman, D. Ban, Nano Energy 26 (2016) 641–647.
[19] J. Sun, Q. Hua, R. Zhou, D. Li, W. Guo, X. Li, G. Hu, C. Shan, Q. Meng, L. Dong, C. Pan, Z.L. Wang, ACS Nano 13 (2019) 4507–4513.
[20] M. Fahim, I. Firdous, W. Zhang, W.A. Daoud, Nano Energy 86 (2021) 106127.
[21] B. Dai, Chem Soc Rev.
[22] Y. Shen, X. Yan, H. Si, P. Lin, Y. Liu, Y. Sun, Y. Zhang, ACS Appl. Mater. Interfaces 8 (2016) 6137–6143.
[23] C. Pan, M. Chen, R. Yu, Q. Yang, Y. Hu, Y. Zhang, Z.L. Wang, Adv. Mater. 28 (2016) 1535–1552.
[24] L. Pan, S. Sun, Y. Chen, P. Wang, J. Wang, X. Zhang, J. Zou, Z.L. Wang, Adv. Energy Mater. 10 (2020) 2000214.
[25] A. Kojima, K. Teshima, Y. Shirai, T. Miyasaka, J. Am. Chem. Soc. 131 (2009) 6050–6051.
[26] Best Research-Cell Efficiency Chart | Photovoltaic Research | NREL, https://www.nrel.gov/pv/cell-efficiency.html, (Accessed 20 June 2024).
[27] Z. Dai, S. Li, X. Liu, M. Chen, C.E. Athanasiou, B.W. Sheldon, H. Gao, P. Guo, N. P. Padture, Adv. Mater. 34 (2022) 2205301.
[28] Z. Li, C. Jia, Z. Wan, J. Xue, J. Cao, M. Zhang, C. Li, J. Shen, C. Zhang, Z. Li, Nat. Commun. 14 (2023) 6451.
[29] J. Briscoe, N. Jalali, P. Woolliams, M. Stewart, P.M. Weaver, M. Cain, S. Dunn, Energy Environ. Sci. 6 (2013) 3035.
[30] J. Briscoe, M. Stewart, M. Vopson, M. Cain, P.M. Weaver, S. Dunn, Adv. Energy Mater. 2 (2012) 1261–1268.
[31] N. Jalali, P. Woolliams, M. Stewart, P.M. Weaver, M.G. Cain, S. Dunn, J. Briscoe, J. Mater. Chem. A 2 (2014) 10945.
[32] S. Lu, J. Qi, Y. Gu, S. Liu, Q. Xu, Z. Wang, Q. Liang, Y. Zhang, Nanoscale 7 (2015) 4461–4467.
[33] H. Chang, Z. Sun, K.Y.-F. Ho, X. Tao, F. Yan, W.-M. Kwok, Z. Zheng, Nanoscale 3 (2011) 258–264.
[34] H.A. Dewi, J. Li, E. Erdenebileg, H. Wang, M. De Bastiani, S. De Wolf, N. Mathews, S. Mhaisalkar, A. Bruno, Sustain. Energy Fuels 6 (2022) 2428–2438.
[35] E. Hernández-Balaguera, B. Romero, M. Najafi, Y. Galagan, Adv. Mater. Interfaces 9 (2022) 2102275.
[36] C. Han, Z. Wei, K. Wang, H. Yu, L. Deng, X. Zhu, H. Yang, X. Sun, F. Zhao, Q. Zhang, Q. Yang, B. Hu, Opt. Express 26 (2018) 26307.
[37] J. Qin, X.-K. Liu, C. Yin, F. Gao, Trends Chem. 3 (2021) 34–46.
[38] C. Zhang, H.-Y. Zhang, H.-Y. Hao, J.-J. Dong, J. Xing, H. Liu, L. Shi, T.-T. Zhong, K.-P. Tang, X. Xu, and School of Mathematics and Physics, China University of Geosciences (Beijing), Beijing 100084, China, Acta Phys. Sin. 69 (2020) 178101.
[39] X. Zhang, L. Zhou, X. Tu, F. Hu, Polyhedron 246 (2023) 116668.